Lian-Ping Wang[1]

Department of Mechanical Engineering,
University of Delaware,
Newark, DE 19716-3140
e-mail: lwang@udel.edu

Oscar G. C. Ardila

School of Mechanical Engineering,
Universidad del Valle,
Cali 12345, Colombia
e-mail: oscar.gerardo.castro@correounivalle.edu.co

Orlando Ayala

Department of Engineering Technology,
Old Dominion University,
Norfolk, VA 23529
e-mail: oayala@odu.edu

Hui Gao

United Technologies Research Center,
East Hartford, CT 06118
e-mail: gaoh@utrc.utc.com

Cheng Peng

Department of Mechanical Engineering,
University of Delaware,
Newark, DE 19716-3140
e-mail: cpengxpp@udel.edu

Study of Local Turbulence Profiles Relative to the Particle Surface in Particle-Laden Turbulent Flows

As particle-resolved simulations (PRSs) of turbulent flows laden with finite-size solid particles become feasible, methods are needed to analyze the simulated flows in order to convert the simulation data to a form useful for model development. In this paper, the focus is on turbulence statistics at the moving fluid–solid interfaces. An averaged governing equation is developed to quantify the radial transport of turbulent kinetic energy when viewed in a frame moving with a solid particle. Using an interface-resolved flow field solved by the lattice Boltzmann method (LBM), we computed each term in the transport equation for a forced, particle-laden, homogeneous isotropic turbulence. The results illustrate the distributions and relative importance of volumetric source and sink terms, as well as pressure work, viscous stress work, and turbulence transport. In a decaying particle-laden flow, the dissipation rate and kinetic energy profiles are found to be self-similar. [DOI: 10.1115/1.4031692]

1 Introduction

Turbulent particle-laden flows are more complicated than their single-phase counterpart owing to a wider range of length and time scales and the additional parameters associated with the dispersed phase [1]. Examples include pneumatic conveying, pulverized coal combustion, spray drying and cooling, particulate pollution control, fluid catalytic cracking, etc. [2,3]. For a turbulent flow laden with nondeforming spherical particles, the length scales range from the particle diameter (d_p) and flow Kolmogorov length (η) to the integral length scale (L). When d_p/η is small and the volume fraction (ϕ_v) of the dispersed phase is low, the response of a particle to the local flow can be well described by an equation of motion [4], making it unnecessary to resolve the disturbance flow on the scale of the particle size. Most theoretical understanding for turbulent particle-laden flows has been developed based on these assumptions.

Computationally, the condition of $d_p/\eta < 1$ partially justifies the use of point-particle-based simulation (PPS) [5]. In the last 25 years, PPS has enabled researchers to discover and quantify a number of important phenomena in turbulent particle-laden flows including preferential concentration [6,7], turbulence modulation by inertial particles [8,9], particle deposition rate, and turbulent collision rate of inertial particles [5,10–13].

In strong turbulent flows where the rate of energy dissipation is high, the flow Kolmogorov scale becomes smaller than the particle size [14]. This introduces finite-size effects greatly complicating the description of the flow system [15,16]. A solid particle can no longer be treated as a point particle. The only rigorous method is to numerically resolve the disturbance flows around solid

particles, which is known as the PRS. PRS of turbulent particle-laden flows requires direct simulation of the turbulent carrier flow and explicit and accurate treatment of many moving fluid–solid interfaces, such that all scales from turbulence integral scale to dissipation scales and particle size are adequately resolved with realistic scale separations that depend on applications.

As a direct numerical simulation tool, PRS is computationally demanding. In recent years, several macroscopic PRS methods based on the Navier–Stokes (N–S) equation have been developed, with the fluid–solid interfaces treated by, for example, the immersed boundary method [17,18], direct-forcing [19,20], local analytical treatment [21], overset grid [14], force-coupling [22], or penalization method [23]. These studies were preliminary in nature, but did contribute to the understanding of flow modulation by the inertial particles and the dynamic effects due to finite particle size.

Alternatively, mesoscopic methods, such as the LBM, have also been developed as a PRS method for turbulent particle-laden flows [24–28]. The LBM approach features a high-level data locality ideal for efficient parallel implementation. Another advantage is that, in LBM, the interactions between the fluid phase and solid particles can be treated as mesoscopic momentum exchange, avoiding the stress integration required for macroscopic approaches [29].

PRS simulations generate more data including statistics at the fluid–solid interfaces. How to condense such data or convert the data into a form that may be useful for model development? How to analyze the flow field where many discrete portions of the space are taken by the solid phase? Some initial attempts to address them are discussed, for example, in Refs. [14,25,30]. Here, we focus on turbulence statistics at the moving solid–fluid interfaces, by examining flow statistics conditioned on the surface of the nearest solid particle. We will make an attempt to derive a transport equation for this purpose and then compute each term in the transport equation from a simulated particle-resolved flow field solved by LBM.

---

[1]Corresponding author.

The paper is organized as follows: In Sec. 2, a brief review of the LBM approach is provided. The radial transport equation conditioned on the particle surface will be derived in Sec. 3. In Sec. 4, we consider three flow configurations and examine the turbulence profiles conditioned on the particle surface and related transport processes. The summary and main conclusions are presented in Sec. 5.

2 Problem Statement and the Particle-Resolved Direct Numerical Simulation (DNS) Approach

2.1 The Lattice Boltzmann Method. Interface-resolved simulations of a turbulent particle-laden flow represent a unique challenge for computational fluid dynamics (CFD). Typical conventional methods are based on solving the macroscopic N–S equations. Here, the turbulent flow with many moving interfaces is simulated by a mesoscopic computational approach known as the LBM. The LBM approach is based on a kinetic formulation and could have certain advantages over the conventional N–S based CFD [31,32]. The basic idea of LBM is to use a kinetic model based on the Boltzmann equation, but retaining the simplest discretized version just sufficient to reproduce the macroscopic N–S equations. There are two drawbacks of LBM, when compared with N–S based CFD: the first is that a larger number of variables (typically 15 or 19 particle distributions at a given lattice point in three-dimensional) need to be solved; the second is a relative lack of experience by the general fluid mechanics community in understanding the accuracy and reliability of the approach and related implementation issues for the type of complex flows we intend to address here. However, these drawbacks are outweighed by its tremendous computational advantages including: (1) quasi-linear nature of the lattice Boltzmann equation, (2) ease of imposing no-slip boundary conditions on solid walls in complex geometry, (3) straightforward coding and parallelization, and (4) flexibilities in incorporating interfacial physics in multiphase flows. For these reasons, LBM models capable of addressing thermal flows, flows through porous media, multiphase flows, electro-osmotic flows, contact line, etc. have been developed and benchmarked in recent years. In this work, we exploit these advantages particularly the ease of imposing boundary conditions on the moving fluid–solid interfaces.

Specifically, the particle-resolved turbulent flows are simulated using the multiple-relaxation-time (MRT) LBM [33], with the details on the treatment of moving fluid–solid interfaces described in Refs. [24,25,34]. Here, we only summarize the essential components of the method.

The MRT LBM solves the evolution of mesoscopic particle distribution function by a lattice Boltzmann equation

$$\mathbf{f}(\mathbf{x} + \mathbf{e}_\alpha \delta t, t + \delta t) = \mathbf{f}(\mathbf{x}, t) - \mathbf{M}^{-1} \cdot \mathbf{S} \cdot [\mathbf{m} - \mathbf{m}^{(eq)}] + \mathbf{Q} \quad (1)$$

where $\mathbf{e}_\alpha$ are microscopic velocities, δt is the lattice time step, $\mathbf{M}$ is an orthogonal transformation matrix converting the distribution function $\mathbf{f}$ from the discrete velocity space to the moment space $\mathbf{m}$, in which the collision relaxation is performed. The term $\mathbf{Q}$ denotes a forcing field in the mesoscopic space to produce a desired nonuniform, time-dependent, large-scale physical space forcing field $\rho_0 \mathbf{q}(\mathbf{x}, t)$. Its implementation follows the MRT formulation [35,36] that is free of low-order discrete lattice errors, and the details were discussed in Ref. [25].

The basic idea of MRT is that the streaming substep is handled in the microscopic lattice-velocity space but the collision substep is performed in the moment space. The transformation between the microscopic velocity space and the moment space is carried out by matrix operations as $\mathbf{m} = \mathbf{M} \cdot \mathbf{f}$, $\mathbf{f} = \mathbf{M}^{-1} \cdot \mathbf{m}$. The diagonal relaxation matrix $\mathbf{S}$ specifies the relaxation rates for the nonconserved moments.

The macroscopic hydrodynamic variables, including density ρ, momentum, and pressure p, are obtained from the moments of the mesoscopic distribution function $\mathbf{f}$. In the nearly incompressible formulation, they are given as

$$\rho = \rho_0 + \delta \rho, \quad \rho_0 = 1 \quad (2)$$

$$\delta \rho = \sum_\alpha f_\alpha, \quad \rho_0 \mathbf{u} = \sum_\alpha f_\alpha \mathbf{e}_\alpha + \frac{\delta t}{2} \rho_0 \mathbf{q}(\mathbf{x}, t), \quad p = \delta \rho c_s^2 \quad (3)$$

where $\mathbf{u}$ is the macroscopic fluid velocity, and the sound speed c_s is equal to $1/\sqrt{3}$ in lattice units. In our implementation, the distribution functions $\mathbf{f}$ are solved only at the fluid lattice nodes.

The design details of the MRT model include three parts. The first part is to choose a proper set of discrete microscopic velocities. The standard D3Q19 model is used here with the following 19 velocities: $\mathbf{e}_0 = (0,0,0)$, $\mathbf{e}_{1,2} = (\pm 1, 0, 0)$, $\mathbf{e}_{3,4} = (0, \pm 1, 0)$, $\mathbf{e}_{5,6} = (0, 0, \pm 1)$, $\mathbf{e}_{7,8,9,10} = (\pm 1, \pm 1, 0)$, $\mathbf{e}_{11,12,13,14} = (\pm 1, 0, \pm 1)$, and $\mathbf{e}_{15,16,17,18} = (0, \pm 1, \pm 1)$. The second part is to specify the 19 orthogonal moments: $\mathbf{m} = (\tilde{\rho}, e, \varepsilon, j_x, q_x, j_y, q_y, j_z, q_z, 3p_{xx}, 3\pi_{xx}, p_{ww}, \pi_{ww}, p_{xy}, p_{yz}, p_{xz}, m_x, m_y, m_z)^{\mathrm{T}}$. These are defined through the elements of the transformation matrix (each subscript runs from 0 to 18) as

$$
\begin{aligned}
&M_{0,\alpha} = ||\mathbf{e}_\alpha||^0, \quad M_{1,\alpha} = 19||\mathbf{e}_\alpha||^2 - 30 \\
&M_{2,\alpha} = (21||\mathbf{e}_\alpha||^4 - 53||\mathbf{e}_\alpha||^2 + 24)/2 \\
&M_{3,\alpha} = e_{\alpha x}, \quad M_{5,\alpha} = e_{\alpha y}, \quad M_{7,\alpha} = e_{\alpha z} \\
&M_{4,\alpha} = (5||\mathbf{e}_\alpha||^2 - 9)e_{\alpha x}, \quad M_{6,\alpha} = (5||\mathbf{e}_\alpha||^2 - 9)e_{\alpha y} \\
&M_{8,\alpha} = (5||\mathbf{e}_\alpha||^2 - 9)e_{\alpha z} \\
&M_{9,\alpha} = 3e_{\alpha x}^2 - ||\mathbf{e}_\alpha||^2, \quad M_{11,\alpha} = e_{\alpha y}^2 - e_{\alpha z}^2 \\
&M_{13,\alpha} = e_{\alpha x}e_{\alpha y}, \quad M_{14,\alpha} = e_{\alpha y}e_{\alpha z}, \quad M_{15,\alpha} = e_{\alpha x}e_{\alpha z} \\
&M_{10,\alpha} = (3||\mathbf{e}_\alpha||^2 - 5)(3e_{\alpha x}^2 - ||\mathbf{e}_\alpha||^2) \\
&M_{12,\alpha} = (3||\mathbf{e}_\alpha||^2 - 5)(e_{\alpha y}^2 - e_{\alpha z}^2) \\
&M_{16,\alpha} = (e_{\alpha y}^2 - e_{\alpha z}^2)e_{\alpha x}, \quad M_{17,\alpha} = (e_{\alpha z}^2 - e_{\alpha x}^2)e_{\alpha y} \\
&M_{18,\alpha} = (e_{\alpha x}^2 - e_{\alpha y}^2)e_{\alpha z}
\end{aligned}
\quad (4)
$$

Then, the Chapman–Enskog multiscaling analysis can be performed on Eq. (1), to formulate the equilibrium moments such that the Euler and N–S equations would be satisfied at the first and second-order, respectively. This will lead to the following results for $\mathbf{m}^{(eq)}$ with a few adjustable parameters:

$$
\begin{aligned}
&\tilde{\rho}^{(eq)} = \tilde{\rho} = \delta\rho, \quad e^{(eq)} = -11\delta\rho + \frac{19}{\rho_0}\left(j_x^2 + j_y^2 + j_z^2\right) \\
&\varepsilon^{(eq)} = \omega_\varepsilon \delta\rho + \frac{\omega_{\varepsilon j}}{\rho_0}\left(j_x^2 + j_y^2 + j_z^2\right) \\
&j_x^{(eq)} = j_x = \rho_0 u_x, \quad j_y^{(eq)} = j_y = \rho_0 u_y, \quad j_z^{(eq)} = j_z = \rho_0 u_z \\
&q_x^{(eq)} = -\frac{2}{3}j_x, \quad q_y^{(eq)} = -\frac{2}{3}j_y, \quad q_z^{(eq)} = -\frac{2}{3}j_z \\
&p_{xx}^{(eq)} = \frac{1}{3\rho_0}\left[2j_x^2 - \left(j_y^2 + j_z^2\right)\right], \quad p_{ww}^{(eq)} = \frac{1}{\rho_0}\left[j_y^2 - j_z^2\right] \\
&p_{xy}^{(eq)} = \frac{1}{\rho_0}j_x j_y, \quad p_{yz}^{(eq)} = \frac{1}{\rho_0}j_y j_z, \quad p_{xz}^{(eq)} = \frac{1}{\rho_0}j_x j_z \\
&\pi_{xx}^{(eq)} = \omega_{xx} p_{xx}^{(eq)}, \quad \pi_{ww}^{(eq)} = \omega_{xx} p_{ww}^{(eq)} \\
&m_x^{(eq)} = m_y^{(eq)} = m_z^{(eq)} = 0
\end{aligned}
\quad (5)
$$

Finally, the relaxation of unconserved moments is described as $\mathbf{S} = \mathrm{diag}(0, s_1, s_2, 0, s_4, 0, s_4, 0, s_4, s_9, s_{10}, s_9, s_{10}, s_{13}, s_{13}, s_{13}, s_{16}, s_{16}, s_{16})$. The kinematic viscosity ν of the model is given as $\nu = (s_9^{-1} - 1)c_s^2 \delta t$.

In this study, the specific model parameters are taken from Ref. [33] with some modification to s_1 and s_{16}, and they are $\omega_\varepsilon = 0.0$, $\omega_{\varepsilon j} = -475/63$, $\omega_{xx} = 0.0$, $s_1 = 1.5$, $s_2 = 1.4$, $s_4 = 1.2$,

$s_9 = \delta t/(3\nu + 0.5\delta t)$, $s_{10} = 1.4$, $s_{13} = s_9$, and $s_{16} = 1.98$. The above completes the description of the D3Q19 MRT LBM model.

2.2 Treatment of Moving Fluid–Solid Interfaces in the LBM Approach. When moving solid particles are present, additional implementation details need to be considered. The no-slip condition at the moving fluid–solid interfaces is treated by a quadratic interpolated bounce-back scheme [37]. In this scheme, the exact location where a lattice link and the solid particle boundary intersect is considered, therefore, the curved solid–fluid interface is explicitly represented. The quadratic interpolation also maintains the second-order accuracy of the LBM approach [29]. When a solid particle moves, a solid lattice node may become a fluid node with unknown distribution functions. The missing distribution functions for the new fluid lattice node are constructed by a newly developed velocity-constrained extrapolation method [29]. The basic idea is to first estimate the missing distribution functions using the three-point normal extrapolation refilling proposed in Ref. [37]. Then, a refinement step is performed to constrain the velocity at the new fluid lattice node to the local solid velocity. This is conveniently carried out within the MRT formulation by transforming the distributions into the moment space, correcting for the momentum, and updating the distributions through an inverse transformation. We find that this constraint can significantly reduce the fluctuations in the hydrodynamic forces when compared to the unconstrained normal extrapolation [29]. Even more importantly, before introducing this constrained scheme, we used equilibrium plus nonequilibrium refilling [38] and encountered numerical instability that causes the code to diverge. After replaced by the velocity-constrained normal extrapolation refilling, our particle-laden turbulent channel flow code has a much better numerical stability.

The hydrodynamic force $\mathbf{F}_i$ and torque $\mathbf{T}_i$ acting on the ith particle are calculated during the interpolated bounce-back procedure by the recently developed Galilean invariant momentum exchange method [29,39]. It is very important that we enforce the local Galilean invariance property in order to produce physically correct results, as discussed in Peng et al. [29]. The particle translational velocity, position, angular velocity, and displacement are then updated as

$$\mathbf{V}_i^{t+\delta t} = \mathbf{V}_i^t + \frac{1}{M_p}\left(\frac{\mathbf{F}_i^{t+\delta t/2} + \mathbf{F}_i^{t-\delta t/2}}{2} + \sum_j \mathbf{F}_{ij}^t\right)\delta t \quad (6)$$

$$\mathbf{Y}_i^{t+\delta t} = \mathbf{Y}_i^t + \frac{1}{2}\left(\mathbf{V}_i^t + \mathbf{V}_i^{t+\delta t}\right)\delta t \quad (7)$$

$$\Omega_i^{t+\delta t} = \Omega_i^t + \frac{1}{I_p}\left(\frac{\mathbf{T}_i^{t+\delta t/2} + \mathbf{T}_i^{t-\delta t/2}}{2}\right)\delta t \quad (8)$$

$$\Theta_i^{t+\delta t} = \Theta_i^t + \frac{1}{2}\left(\Omega_i^t + \Omega_i^{t+\delta t}\right)\delta t \quad (9)$$

where M_p and $I_p \equiv \frac{2}{5}M_p R_i^2$ are the mass and moment of inertia of the ith particle, R_i is the particle radius, and $\mathbf{F}_{ij}$ represents unresolved interaction force acting on the ith particle due to its interaction with jth particle (e.g., the lubrication force correction, see Refs. [40,41]). In this study, a simple pairwise repulsive force model, same as what was used in Ref. [24], is applied to prevent particles from overlapping.

In summary, the LBM approach is a mesoscopic method that has been shown to be capable of simulating both single-phase and particle-laden turbulent flows with solid particles explicitly resolved. The accuracy of the method has been validated by comparing results to pseudospectral and finite-difference methods [28,42].

3 The Kinetic Energy Equation Relative to a Moving Solid Particle

In this section, we shall derive a Reynolds-averaged like equation for turbulent kinetic energy, with spatial coordinates relative to the surface of a solid particle, assuming the solid particle is suspended in a stationary forced turbulent flow. We take two frames of reference, a fixed inertial frame and a moving particle frame that translates with the center velocity $\mathbf{V}(t) = d\mathbf{Y}(t)/dt$ of the selected solid particle, where $\mathbf{Y}(t)$ is the location of the center of the solid particle. The moving particle frame does not rotate although the solid particle might do. A spatial point is indicated by $\tilde{\mathbf{x}} = (\tilde{x}_1, \tilde{x}_2, \tilde{x}_3)$ in the fixed frame, and $\tilde{\mathbf{x}} = \mathbf{Y}(t) + \mathbf{x}$, where $\mathbf{x} = (x_1, x_2, x_3)$ is the coordinates in the moving particle frame. The same clock is used in the two frames so $\tilde{t} = t$. The local fluid velocity $\tilde{\mathbf{u}}$ in the fixed frame can be expressed as $\tilde{\mathbf{u}}(\tilde{\mathbf{x}}, \tilde{t}) = u_j(\mathbf{x}, t) + V_j(t)$, where $\mathbf{u}$ is the fluid velocity in the moving frame.

The transformation from the fixed frame to the moving frame can be made by noting that

$$\frac{\partial}{\partial\tilde{t}} = \frac{\partial}{\partial t} - V_j\frac{\partial}{\partial x_j}, \quad \frac{\partial}{\partial\tilde{x}_j} = \frac{\partial}{\partial x_j} \quad (10)$$

Then, the incompressible continuity equation and N–S equation in the moving frame are

$$\frac{\partial u_k}{\partial x_k} = 0 \quad (11)$$

$$\frac{\partial u_n}{\partial t} + u_k\frac{\partial u_n}{\partial x_k} = -\frac{1}{\rho_f}\frac{\partial p}{\partial x_n} + \nu\frac{\partial^2 u_n}{\partial x_k \partial x_k} + q_n - \frac{dV_n}{dt} \quad (12)$$

where $\mathbf{q}$ is the body force per unit mass and p is the pressure. It follows that the kinetic energy equation in the moving frame can be written as:

$$\frac{\partial\left(\frac{1}{2}u^2\right)}{\partial t} + u_k\frac{\partial\left(\frac{1}{2}u^2\right)}{\partial x_k} = -\frac{\partial}{\partial x_j}\left(u_j\frac{p}{\rho_f}\right) - \frac{V_j}{\rho_f}\frac{\partial p}{\partial x_j} - \varepsilon + \frac{\partial}{\partial x_j}(2\nu u_k e_{jk})$$
$$+ u_j q_j + V_j q_j - \frac{d\left(\frac{1}{2}V^2\right)}{dt} - \frac{\partial(u_m V_m)}{\partial t} - u_k\frac{\partial(u_m V_m)}{\partial x_k}$$
$$(13)$$

where the rate of strain and the dissipation rate per unit mass are

$$\tilde{e}_{jk} = e_{jk} = \frac{1}{2}\left(\frac{\partial u_j}{\partial x_k} + \frac{\partial u_k}{\partial x_j}\right), \quad \tilde{\varepsilon} = \varepsilon \equiv 2\nu e_{jk}e_{jk} \quad (14)$$

and they are frame-independent.

Our next step is to write down properly the averaged equation around a solid particle. Here, a triple averaging process is possible: First, we take a frame of reference that is moving with the nearest solid particle (i.e., the reference particle), and a spatial point is associated with this nearest particle using a local spherical coordinate system (r, θ, ϕ), with r being the distance from the center of the reference particle, θ is the polar angle, say defined with respect to a fixed orientation, and ϕ is the azimuthal angle. The first average is over θ and ϕ. The second averaging is over all reference particles. Finally, the third averaging is over time if the flow is statistically stationary. These three averages will be denoted as $\langle\rangle^S$, $\langle\rangle^P$, and $\langle\rangle^T$, respectively.

Consider the advection term. Rewriting in local spherical coordinates, we have

$$u_k\frac{\partial\left(\frac{1}{2}u^2\right)}{\partial x_k} = \frac{\partial\left(u_k\frac{1}{2}u^2\right)}{\partial x_k} = \frac{1}{r^2}\frac{\partial}{\partial r}\left[r^2\left(u_r\frac{1}{2}u^2\right)\right]$$
$$+ \frac{1}{r\sin\theta}\frac{\partial}{\partial\theta}\left[\left(u_\theta\frac{1}{2}u^2\right)\sin\theta\right] + \frac{1}{r\sin\theta}\frac{\partial\left(u_\psi\frac{1}{2}u^2\right)}{\partial\phi}$$
$$(15)$$

Performing the averaging over θ and ϕ, namely,

$$\langle\cdots\rangle^S \equiv \frac{1}{4\pi}\int_0^\pi \sin\theta d\theta \int_0^{2\pi} d\phi(\cdots) \qquad (16)$$

yields

$$\left\langle u_k \frac{\partial\left(\frac{1}{2}u^2\right)}{\partial x_k}\right\rangle^S = \frac{1}{r^2}\frac{\partial}{\partial r}\left(r^2\left\langle u_r\frac{1}{2}u^2\right\rangle^S\right)$$
$$+\frac{1}{r}\frac{1}{4\pi}\int_0^{2\pi}d\phi\left[\left(\left(u_\theta\frac{1}{2}u^2\right)\sin\theta\right)_{\theta=\pi}-\left(\left(u_\theta\frac{1}{2}u^2\right)\sin\theta\right)_{\theta=0}\right]$$
$$+\frac{1}{r}\frac{1}{4\pi}\int_0^\pi d\theta\left[\left(u_\phi\frac{1}{2}u^2\right)\Big|_{\phi=2\pi}-\left(u_\phi\frac{1}{2}u^2\right)\Big|_{\phi=0}\right]$$
$$=\frac{1}{r^2}\frac{\partial}{\partial r}\left(r^2\left\langle u_r\frac{1}{2}u^2\right\rangle^S\right) \qquad (17)$$

Clearly, the continuity equation, after the above average, can be written as

$$\frac{1}{r^2}\frac{\partial}{\partial r}\left(r^2\langle u_r\rangle^S\right)=0 \qquad (18)$$

Together with the no-slip boundary condition, we can obtain that

$$\langle u_r\rangle^S=0 \qquad (19)$$

By symmetry considerations (there is no physical reason for the relative fluid motion to go along one direction relative to the opposite direction on a given r surface), for homogeneous isotropic flow, one could argue that

$$\langle u_\theta\rangle^S=0, \quad \langle u_\phi\rangle^S=0 \qquad (20)$$

Therefore, one can view that all velocity components have no mean when averaged over a given r surface, or all kinetic energy comes from the turbulent fluctuations of velocity. Therefore, hereafter, u_r, u_θ, and u_ϕ are viewed as the fluctuation velocity component in the respective direction of the spherical coordinates. It follows that the term in Eq. (17) is interpreted as the turbulent transport of kinetic energy by the radial velocity fluctuations. The left-hand side of Eq. (13) can now be written as

$$\frac{\partial}{\partial t}\left\langle\frac{1}{2}u^2\right\rangle^{SP}+\frac{1}{r^2}\frac{\partial}{\partial r}\left(r^2\left\langle u_r\frac{1}{2}u^2\right\rangle^{SP}\right)=\cdots \qquad (21)$$

Applying the same averaging process to each term on the right-hand side of Eq. (13), we can obtain the following governing equation of the averaged local kinetic energy equation in the moving frame:

$$\left\langle\frac{\partial}{\partial t}\left\langle\frac{1}{2}u^2\right\rangle^{SP}\right\rangle^T=-\left[\frac{1}{r^2}\frac{\partial}{\partial r}\left(r^2\left\langle u_r\frac{1}{2}u^2\right\rangle^{SPT}\right)\right]-\frac{1}{r^2}\frac{\partial}{\partial r}\left(r^2\langle u_r\mathbf{u}\cdot\mathbf{V}\rangle^{SPT}\right)$$
$$-\left[\frac{1}{r^2}\frac{\partial}{\partial r}\left(\frac{r^2}{\rho_f}\langle(u_r+V_r)P\rangle^{SPT}\right)\right]+\left[\frac{1}{r^2}\frac{\partial}{\partial r}\left(r^2\langle 2\nu\mathbf{u}\cdot\mathbf{e}\rangle^{SPT}\right)\right]$$
$$-\langle\varepsilon\rangle^{SPT}$$
$$+\langle\mathbf{u}\cdot\mathbf{q}\rangle^{SPT}+\langle\mathbf{V}\cdot\mathbf{q}\rangle^{SPT} \qquad (22)$$

The terms on the right-hand side, from top to bottom, represent, respectively, (1) the net turbulent transport (by flow relative to the solid particle) of the kinetic energy in the radial direction (the relative transport in short); (2) the net transport of cross energy ($\mathbf{u}\cdot\mathbf{V}$) in the radial direction relative to the solid particle (the transport of cross-energy in short); (3) the rate of work done on the boundaries of the spherical shells by pressure (the pressure work in short); (4) the rate of work done on the boundaries of the

spherical shells by the shear stress (the viscous stress work in short); (5) the rate of local viscous dissipation per unit mass (the viscous dissipation in short); (6) the rate of energy input by forcing associated with the relative fluid motion; and (7) the rate of forcing energy input associated with the particle velocity.

Alternatively, assuming a thin spherical shell of width dr (and the volume $dV_{\text{Shell}}=4\pi[(r+dr)^3-r^3]/3\approx 4\pi r^2 dr$), we can write

$$0=\left(4\pi r^2\left\langle u_r\frac{1}{2}u^2\right\rangle^{SPT}\right)_r-\left(4\pi r^2\left\langle u_r\frac{1}{2}u^2\right\rangle^{SPT}\right)_{r+dr}$$
$$+\left(4\pi r^2\langle u_r\mathbf{u}\cdot\mathbf{V}\rangle^{SPT}\right)_r-\left(4\pi r^2\langle u_r\mathbf{u}\cdot\mathbf{V}\rangle^{SPT}\right)_{r+dr}$$
$$+\left[4\pi r^2\left\langle\frac{-p(u_r+V_r)}{\rho_f}\right\rangle^{SPT}\right]_{r+dr}-\left[4\pi r^2\left\langle\frac{-p(u_r+V_r)}{\rho_f}\right\rangle^{SPT}\right]_r$$
$$+\left[4\pi r^2\langle 2\nu\mathbf{u}\cdot\mathbf{e}\rangle^{SPT}\right]_{r+dr}-\left[4\pi r^2\langle 2\nu\mathbf{u}\cdot\mathbf{e}\rangle^{SPT}\right]_r$$
$$-\langle\varepsilon\rangle^{SPT}dV_{\text{shell}}+\langle\mathbf{u}\cdot\mathbf{q}\rangle^{SPT}dV_{\text{shell}}+\langle\mathbf{V}\cdot\mathbf{q}\rangle^{SPT}dV_{\text{shell}} \qquad (23)$$

The above-averaged equation ignores the orientational dependence of conditional statistics relative to the effective slip motion, thus represents only a first step toward understanding the turbulence modulation by finite-size particles. The nature of the conditional average differs from the typical volume average [16,43] or probability density function (PDF)-based descriptions [44] used in the multiphase flow literature. From the point of view of the Reynolds-Averaged Navier–Stokes (RANS) equations, the overall statistical average of an interested quantity for a stationary homogeneous isotropic particle-laden flow can be written as

$$F^{\text{RANS}} = V_f \int_0^{r_{\max}} F^{SPT}(r) f(r) dr \qquad (24)$$

where $F^{SPT}(r)$ is the conditional average, $f(r)$ is the probability distribution function of spatial position at a distance r from a solid–fluid interface (e.g., see Fig. 10(a)), and $V_f = (1 - \theta)V$ is the volume occupied by the fluid. Here, θ is the particle volume fraction and V is the total volume.

We shall examine each term in Sec. 4.2 for a stationary particle-laden turbulent flow for which the term on the left-hand side is zero.

4 Results

In this section, we consider three different flow configurations: (1) a decaying turbulence passing over a fixed particle, (2) a forced, particle-laden, homogeneous, and isotropic turbulence, and (3) a decaying particle-laden, homogeneous, and isotropic turbulence. The main discussions will be on the local turbulence profiles conditioned a solid particle surface, as a alternative way to gauge the effects of finite-size solid particles on the carrier-phase turbulence. The first case was investigated by Burton and Eaton [14] using a finite-difference method together with an overset-grid technique. Therefore, a comparison with their data serves as a validation of our mesoscopic approach.

4.1 Decaying Turbulence Passing Over a Fixed Particle. Here, we consider a decaying homogeneous isotropic turbulence passing over a fixed solid particle, focusing on turbulence modulation in the region near the particle. The parameters are similar to those used in Ref. [14]. In the simulation, we utilize a domain of 512^3 grid points with periodic boundary conditions applied in all three directions. An initial turbulent field is obtained by specifying a Gaussian field with a prescribed kinetic energy spectrum as in Ref. [14]

$$E(k) = \left(\frac{6u_0^2}{\sqrt{\pi}}\right)\left(\frac{k^2}{k_p^3}\right)\exp\left[-\left(\frac{k}{k_p}\right)^2\right] \qquad (25)$$

where k is the wave number, k_p is the wave number at which $E(k)$ reaches a maximum, and u_0 is the initial rms velocity. Both k and k_p have been normalized by the minimum wavenumber $k_0 \equiv 2\pi/L_B$, where L_B is the computational domain size. The initial flow statistics can be derived from Eq. (25) as follows:

$$\frac{3}{2}u_{\text{rms}}^2 \equiv \int_0^\infty E(k)dk = \frac{3}{2}u_0^2 \quad \text{or} \quad \frac{u_{\text{rms}}}{u_0} = 1.0 \qquad (26)$$

$$\frac{\langle\varepsilon\rangle L_B}{u_0^3} \equiv \frac{2\nu L_B}{u_0^3}\int_0^\infty k^2 E(k)dk = 18\pi^2 k_p^2 \frac{\nu}{u_0 L_B} \qquad (27)$$

$$\frac{L_f}{L_B} \equiv \frac{\pi}{2u_0^2 L_B}\int_0^\infty \frac{E(k)}{k}dk = \frac{3}{4\sqrt{\pi}k_p} \qquad (28)$$

$$\frac{\lambda}{L_B} \equiv \frac{1}{L_B}\sqrt{\frac{15\nu u_0^2}{\langle\varepsilon\rangle}} = \frac{1}{2\pi k_p}\sqrt{\frac{10}{3}} \qquad (29)$$

$$\frac{\eta}{L_B} \equiv \frac{1}{L_B}\left(\frac{\nu^3}{\langle\varepsilon\rangle}\right)^{1/4} = \sqrt{\frac{1}{3\pi\sqrt{2}}\frac{1}{k_p}\frac{\nu}{u_0 L_B}} \qquad (30)$$

$$R_\lambda \equiv \frac{u_{\text{rms}}\lambda}{\nu} = \frac{1}{2\pi k_p}\sqrt{\frac{10}{3}}\frac{u_0 L_B}{\nu} \qquad (31)$$

where u_{rms} is the realized component rms fluctuation velocity, ν is the fluid kinematic viscosity, ε is the viscous dissipation rate, L_f is the longitudinal velocity correlation length, λ is the transverse Taylor microscale, η is the Kolmogorov length, and R_λ is the Taylor microscale Reynolds number. It is noted that the peak wavenumber k_p can be derived from the definitions of R_λ and η above

$$k_p = \left(\frac{L_B}{2\pi}\right)\left(\frac{20}{27R_\lambda^2\eta^4}\right)^{1/4} \qquad (32)$$

After the initialization of the velocity field, the populations $\mathbf{f}(\mathbf{x}, t)$ were then evolved iteratively to establish a consistent initial

Table 1 Parameter settings for flow field initialization in our LBM code and in the finite-difference simulation of Burton and Eaton [14]

	Grid	L_B	L_B/d	u_0	k_p/k_0	ν	R_λ	η/d_p
LBM	512^3	512	64	0.0205	2.34	0.0193	64.34	0.48
BE [14]	192^3	192	192	0.447	7.03	0.122	65	0.5

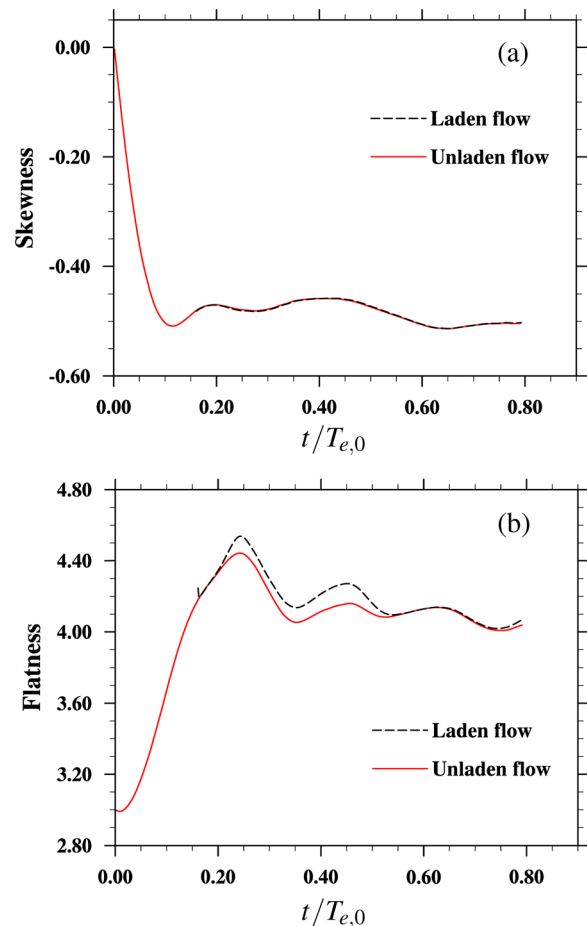Here, d_p is the particle diameter.

Fig. 1 Time evolution of high-order statistics of turbulence for both particle-laden and unladen flow: (a) skewness and (b) flatness

pressure field as described in Mei et al. [45]. The parameter settings are shown in Table 1. The particle radius is set to four lattice units in our simulation. Here, we set the same input parameters in our simulation as those in Ref. [14], i.e., the same Taylor microscale Reynolds number R_λ and the ratio between the Kolmogorov length and particle diameter η/d. Note that due to the reduced size of our computational domain ($L_B/d = 64$ as compared to 192 in Ref. [14]), the normalized peak wavenumber k_p/k_0 in our simulation is consequently decreased in order to maintain the same R_λ and η/d as in Ref. [14]. Nevertheless, the domain size L_B of our LBM simulation is verified to be larger than four times the integral length L_f, which is 92.16 in the lattice Boltzmann units at $t = 0$, implying it is sufficient to accommodate the largest length scale of the turbulence at the specified Taylor microscale Reynolds number R_λ.

The total time duration of our LBM simulation is from $t = 0$ to $t = 0.79T_{e,0}$, corresponding to 10,000 time steps, where the initial eddy turnover time is defined as $T_{e,0} \equiv u_{\mathrm{rms}}^2/\varepsilon$. The high-order statistics of turbulence is realized by evolving the single-phase initial random flow until the skewness of about -0.5 has been developed at $t = 0.16T_{e,0}$, as shown in Fig. 1(a). At this point, a single fixed particle with diameter of about twice the Kolmogorov length scale of the unladen turbulence is inserted at the center of the domain.

No-slip boundary condition on the particle surface is achieved by applying a second-order interpolated bounce-back scheme. For the fixed particle, the information of the populations $\mathbf{f}(\mathbf{x}, t)$ for the fluid nodes inside the particle is ignored. The flow field is over-resolved as shown by $k_{\max}\eta > 10$ for the whole time interval.

Figure 2 displays zoom-in view of the vorticity contours on a center-cut plane of $z = 255.5$. Both the laden and unladen flows are shown at two time instants of $0.47T_{e,0}$ (6000 lattice time steps) and $0.79T_{e,0}$ (10,000 lattice time steps), respectively. The enhanced vorticity near the particle surface indicates the local increase of dissipation, which can be attributed to the effect of the no-slip boundary condition on the particle surface. At large radial distance from the particle surface, the particle-laden flow is almost identical with the unladen flow results.

Figures 1 and 3 illustrate the impact of particle insertion on turbulence evolution using various statistics, including the velocity derivative skewness and flatness, Taylor microscale Reynolds number, and normalized turbulent dissipation rate. Due to the small volume fraction of 2.0×10^{-6}, the particle-laden flow is almost indistinguishable from the unladen flow, except for the flatness shown in Fig. 1(b), where the two cases are distinct from the moment of particle insertion at $t = 0.16T_{e,0}$ to $t = 0.55T_{e,0}$, corresponding to 2000–7000 lattice time units, which likely scales
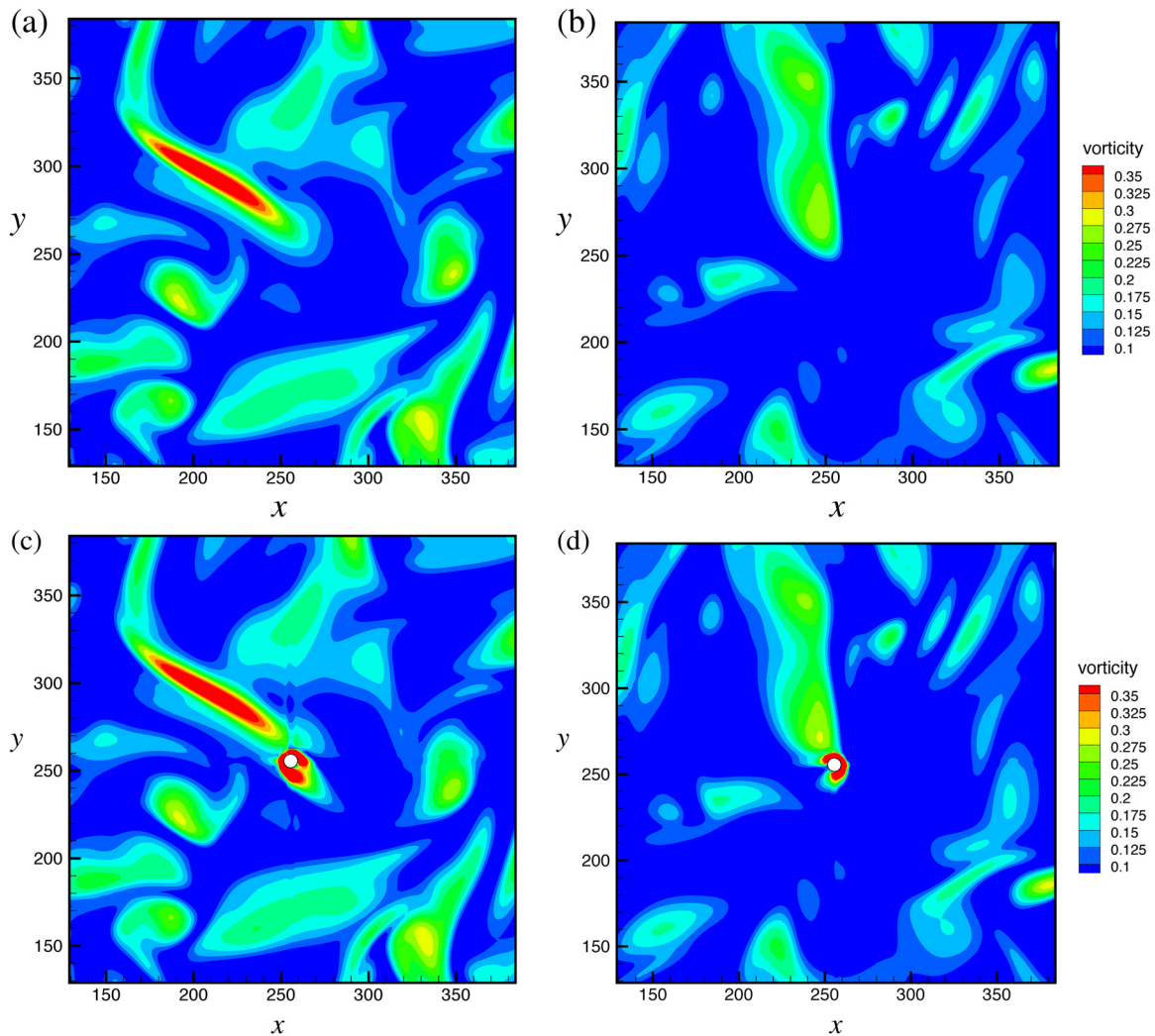

Fig. 2 Zoom-in view of vorticity contour and particle location on a plane-cut of $z = 255.5$ in the 512^3 simulation: (*c*) $0.47T_{e,0}$ and (*d*) $0.79T_{e,0}$. Note that the presence of particles is associated with high vorticity values (represented by the colors toward the red end in the online version (or the dark end in black and white)), indicating relatively large dissipation near particle surfaces. The corresponding vorticity contours for single-phase flow at the two times are shown in (*a*) and (*b*), respectively.
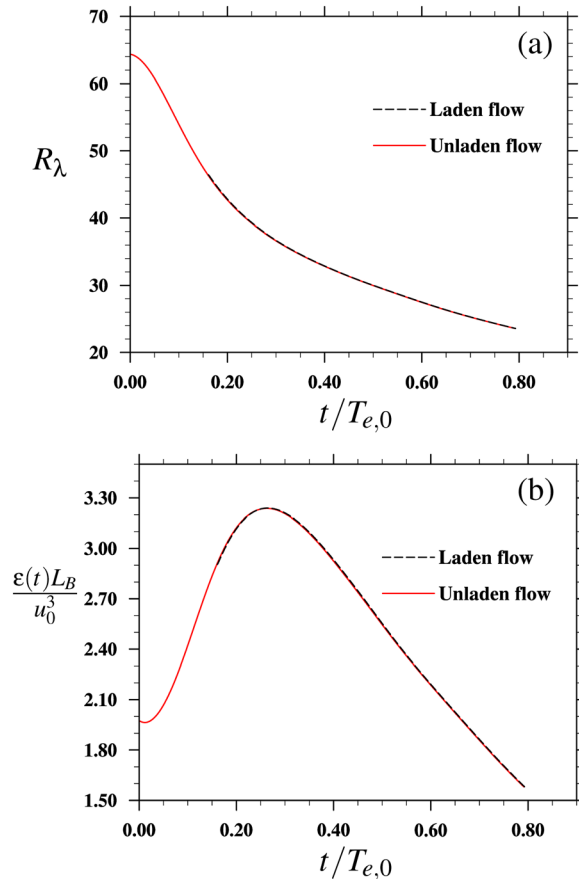
Fig. 3 Time evolution of (*a*) Taylor microscale Reynolds number and (*b*) normalized dissipation rate for both particle-laden and unladen flow

Fig. 4 Normalized (*a*) dissipation rate and (*b*) turbulent kinetic energy as a function of distance from the center of the solid particle. The horizontal line marks the level of 1.0.

as the large-eddy turnover time at the moment of particle insertion. There is also a fast adjustment at the moment of particle insertion (the sudden drop of flatness). The fast adjustment time can be roughly estimated as $T_\delta = \delta_{BL}^2/\nu$, where the boundary layer thickness $\delta_{BL} \sim a_p/\sqrt{\mathrm{Re}_p}$, and ν is the fluid kinematic viscosity. In this case, the maximum particle Reynolds number Re_p is approximately 20 [14]. Then, $T_\delta \sim a_p^2/(\mathrm{Re}_p \nu) = 4^2/(20 \times 0.0193) = 41.5$ or $T_\delta/T_{e,0} = 0.0033$. After this time duration, the flatness of the laden flow and unladen flow reconciles.

Figure 4 shows the averaged local profiles of dissipation rate and turbulent kinetic energy as a function of distance from the particle center, which is calculated by volume-average in spherical shells around the particle. The strain rate s_{ij} was computed in terms of nonequilibrium moments [46]. The particle-laden flow results were first normalized by their unladen counterparts, and then averaged over time to produce a mean profile. Specifically, in this study, we picked the normalized profiles at 7000, 8000, 9000, and 10,000 lattice time units, which is after the flow adjustment period described in Fig. 1(*b*) and consequently allow us to avoid the transient effect introduced by the particle insertion. The four time instants also correspond to $t = 0.66T_{e,i}, 0.80T_{e,i},$ $0.93T_{e,i}$, and $1.06T_{e,i}$, respectively, where $T_{e,i}$ is the eddy turnover time estimated at the moment when particle is inserted into the domain and is 7540 lattice time units. The time-averaged profiles are then compared with the results in Ref. [14], where the data were processed in a similar manner. Note that the temporal average performed for Burton and Eaton's data is from $t = 0.71T_{e,i}$ to $1.07T_{e,i}$ in their case, which covers approximately the same time duration as in our simulation.

Considering the different configurations in our LBM simulation and the overset-grid finite-difference simulation in Burton and Eaton [14], it is interesting to observe that the results from the two
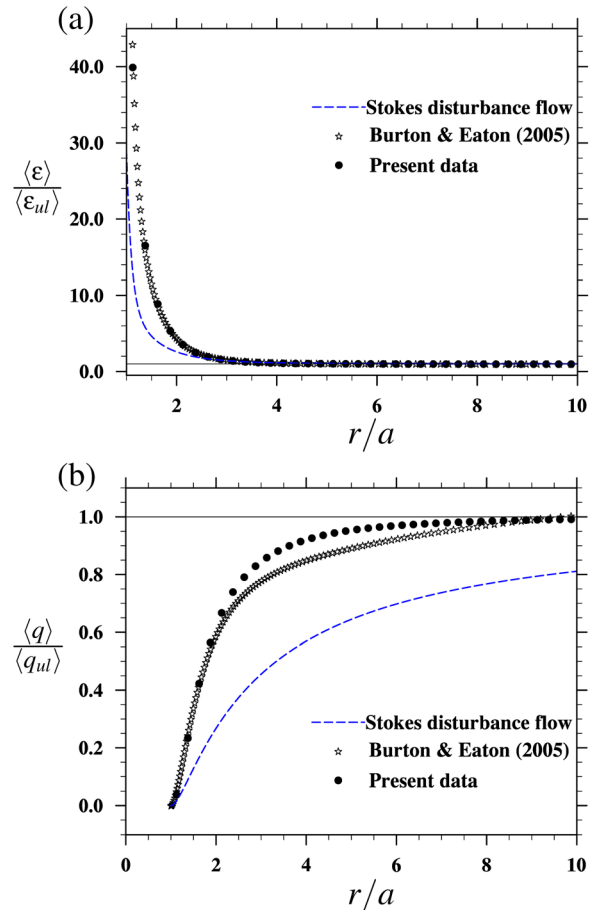
fundamentally different (mesoscopic versus macroscopic) methods reach quantitative agreement. Our dissipation rate profile shown in Fig. 4(*a*) is almost identical to the results of Burton and Eaton [14], where its value drops to within 20% of unit value prior to $r/a_p < 4$ and then flat out to unit value toward large radial distance. For the turbulent kinetic energy profiles shown in Fig. 4(*b*), the overlapped data within the range of $1.0 < r/a_p < 1.5$ depict a substantial increase from zero to about 0.6, followed by a gradual recovery toward full turbulent kinetic energy within the range of $1.5 < r/a_p < 9$, where the LBM results show marginally higher kinetic energy in this interval. This difference is related to the use of a much smaller computational domain size in our simulation. Overall, it is clear that the turbulence has been attenuated significantly near the particle surface. In this case, the turbulent kinetic energy is zero on the surface of solid particle. Additionally, a zeroth-order analytic model based on the Stokes disturbance flow (see the Appendix) is also presented in Fig. 4, to be compared with the simulation results. The model prediction shows a smaller kinetic energy and dissipation rate, which can be ascribed to the effect of finite particle Reynolds number in the simulation, such that the disturbance flow around the particle is not a Stokes flow and the contributions due to the background turbulence.

4.2 Stationary Particle-Laden Turbulence. We next consider a forced homogeneous and isotropic turbulence laden with monodisperse, nonsedimenting solid particles simulated in Ref. [25]. The case considered here is the case labeled as LB256HRP in Ref. [25]. The particle radius is set to four lattice units in the simulation. The domain size is about 257.5 Kolmogorov lengths or five longitudinal integral lengths (see Table 2 in Ref. [25]). The
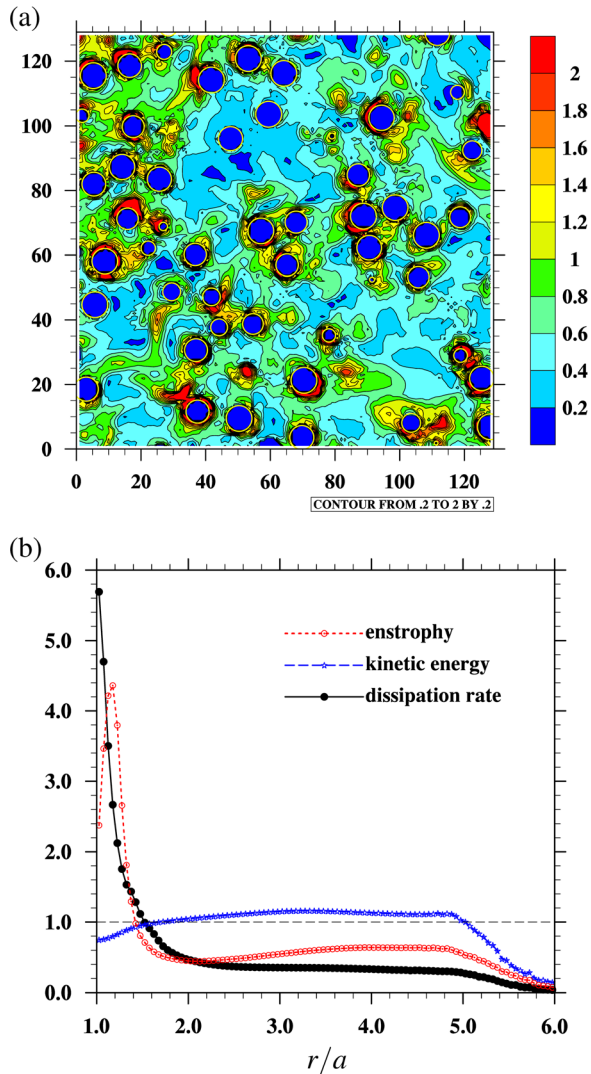
(a)

CONTOUR FROM .2 TO 2 BY .2

(b)

Fig. 5 (*a*) Contour of the normalized local strain rate defined as $\sqrt{\varepsilon/\langle\varepsilon\rangle}^{\text{fluid}}$ and particle positions in an *x–y* plane at *z* = 128.5, from a PRS of three-dimensional, particle-laden, forced homogeneous isotropic turbulence. This figure is taken from Ref. [25]. Only a quarter of the plane is shown. (*b*) Profiles conditioned on the particle surface. Each is normalized by its respective field mean.

particle volume fraction is about 10%, particle-to-fluid density ratio is five, and the particle diameter is eight times the flow Kolmogorov scale. The Taylor microscale Reynolds number of the particle-laden turbulence is 45. At this volume fraction, the ratio of the averaged particle center-to-center distance l_p to the particle radius a_p is $l_p/a_p = (4\pi/3\phi_v)^{1/3} \approx 3.47$. It is found that the measured dimensionless flow dissipation rate in the particle-laden turbulence is 2.35 times the value in the unladen (i.e., single-phase) turbulence, due to both reduction of the effective flow Reynolds number and the viscous boundary layer on the surfaces of solid particles. The thickness of the boundary layer is found to be about $0.4a_p$, where a is the particle radius. Regions of large local dissipation often occur near the surface of a solid particle (Fig. 5(*a*)). In the spectral space, presence of solid particles attenuates energy at large scales including the forcing shells and augments energy at the small scales.

Here, we focus on the local profiles conditioned on the particle surface. Figure 5(*b*) shows the averaged profiles, applying triple averaging as described in Sec. 3, of local dissipation rate, kinetic energy, and enstrophy (the squared vorticity). Here, r is measured
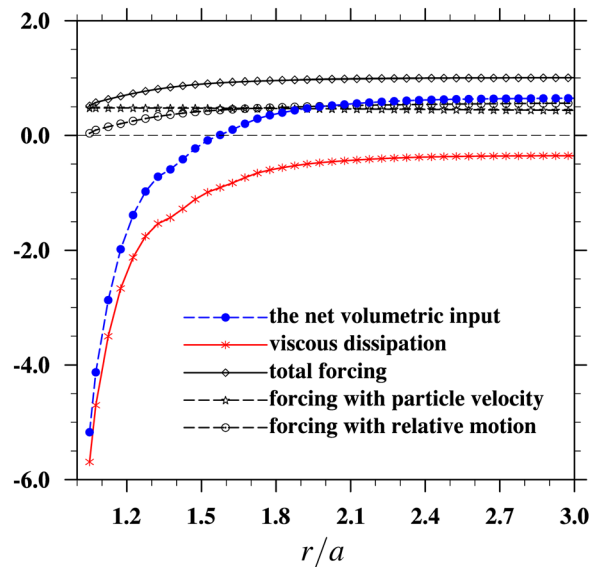

Fig. 6 Profiles of volumetric source and sink terms conditioned on the particle surface. All quantities are normalized by the fluid-phase average dissipation rate.
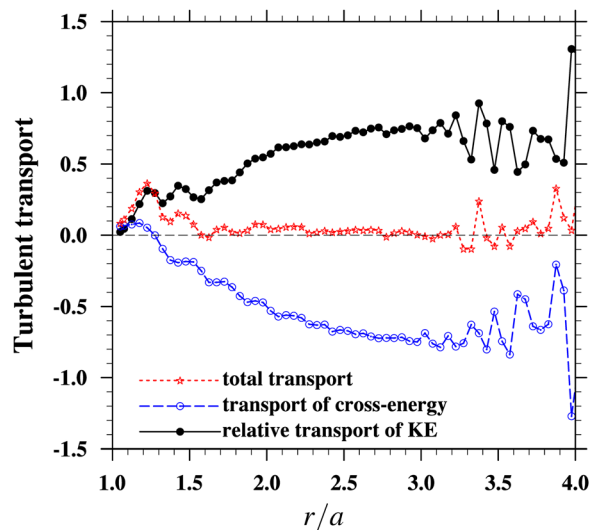

Fig. 7 Profiles of turbulent transport terms conditioned on the particle surface. All quantities are normalized by the fluid-phase average dissipation rate.

from the center of the nearest solid particle. In computing the conditioned value, we divide the distance relative to the nearest particle center into equal bins with a bin width equal to $0.05a_p$, and the average value is computed based on all fluid node points that fall into a given bin. Each quantity is normalized by its respective phase mean. Since they are averaged over a period of 200,000 time steps or about 138 eddy turnover times, they are more accurate in the large r/a_p region than those shown in Figs. 8–10 in Ref. [25]. The average dissipation rate is peaked at the surface of a solid particle, which makes a significant contribution to the field mean dissipation. The enstrophy is peaked at a location $0.175a_p$ from the solid particle surface, partially associated with local flow separation and vortex shedding. A local minimum in enstrophy occurs at $(r/a_p - 1) = 1.075a_p$. The local kinetic energy on the particle surface is less than the mean value, due to the larger particle density and finite particle size. The nonuniform profiles shown in Fig. 5(*b*) imply that the kinetic energy is transported from the bulk flow regions (away from the solid particles) to the particle surfaces, where it is dissipated more rapidly.
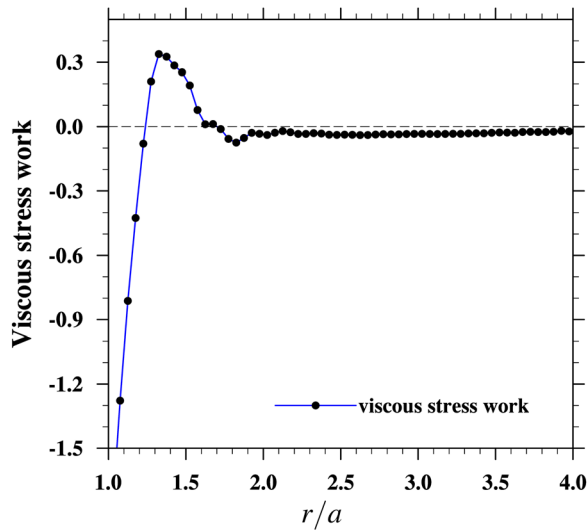
Fig. 8 Profile of viscous stress work conditioned on the particle surface. It is normalized by the fluid-phase average dissipation rate.
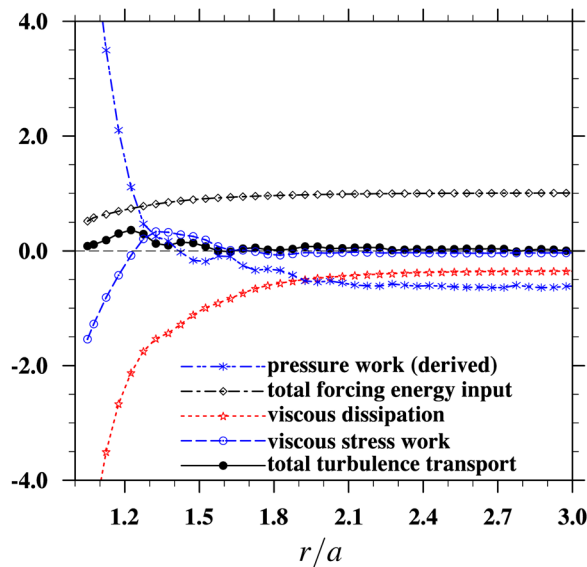

Fig. 9 Profiles of the pressure work and other terms in the balance equation (Eq. (22)). All quantities are normalized by the fluid-phase average dissipation rate.

Fig. 10 (*a*) The PDF of the bin node numbers and (*b*) a replot of Fig. 9 when weighted by the PDF in (*a*)

Table 2 Parameters for the decaying particle-laden flow simulations at the particle release time

Case	N^3	d	ρ_p/ρ_f	N_p	d/η	d/λ	ϕ_v	ϕ_m	τ_p/τ_k
3	256^3	8.0	5.0	6400	16.1	1.1	0.10	0.36	71.9
3H	512^3	16.0	5.0	6400	16.1	1.1	0.10	0.36	71.9

According to Sec. 3, this radial transport is caused by several mechanisms including the pressure work, viscous stress work, and turbulent transport. For the laminar Stokes disturbance flow, the Appendix shows that both the pressure work and the viscous stress work transport the kinetic energy into the near surface regions to balance with the viscous dissipation, with the pressure work providing one-third of the net input, and the viscous work the remaining two-thirds. We shall now examine each of the terms in the kinetic energy transport equation (Eq. (22)).

We shall first examine the volumetric source and sink terms, namely, the last three terms, in Eq. (22). Figure 6 shows the dissipation term (with the minus sign included), the forcing input associated with the relative motion $\langle \mathbf{u} \cdot \mathbf{q} \rangle^{SPT}$, and the forcing input associated with the particle velocity $\langle \mathbf{V} \cdot \mathbf{q} \rangle^{SPT}$. All quantities are normalized by the fluid-phase average dissipation rate (see below). We observe that while the dissipation term extracts the kinetic energy, the two forcing terms are both positive and adds
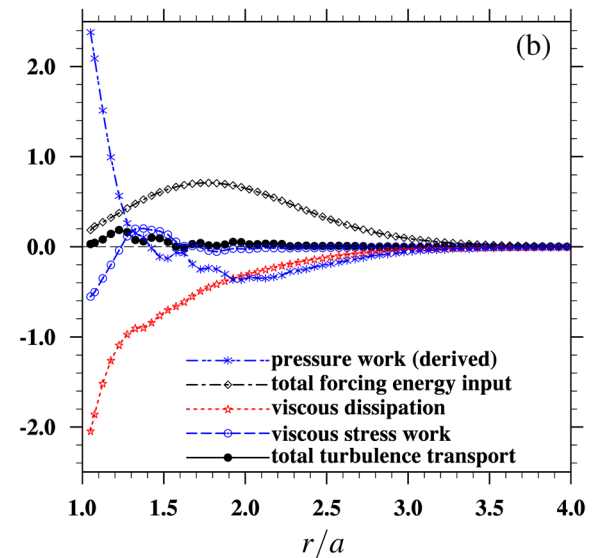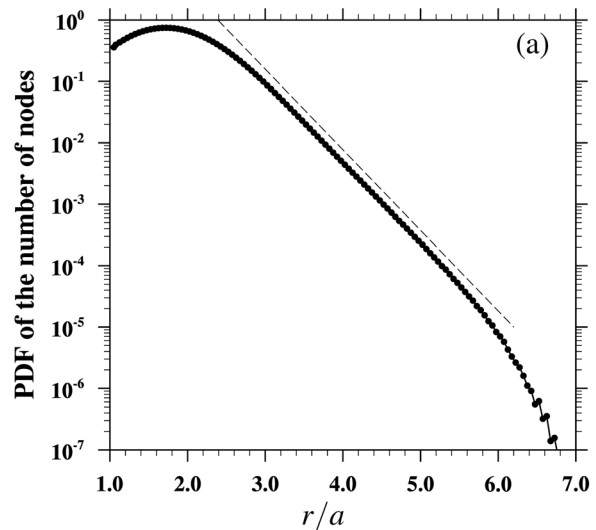
the kinetic energy. The forcing associated with the particle velocity is nearly constant, while the forcing associated with the relative fluid velocity increases with r. The volume-integrated value of the two forcing terms together is 9.33 in LBM units, while the volume-integrated value of dissipation rate is 10.20, showing a rough balance between the two. Here, the volume-integrated value of a quantity is its conditioned value in a bin times the number of node points falling into the bin, summed over all bins. Since $\langle \varepsilon \rangle^{\text{fluid}} V(1 - \phi_v) = 10.20$ in the LBM units, where $\langle \varepsilon \rangle^{\text{fluid}}$ is the average local dissipation in the fluid, $V = 256^3$ is the total volume, $\phi_v = 0.102$, giving $\langle \varepsilon \rangle^{\text{fluid}} = 6.77 \times 10^{-7}$ in LBM units. This is the value we use to normalize all quantities in Figs. 6–9. Also shown is the sum of the two forcing inputs and the dissipation term, namely, the net volumetric input. It is positive for $r > 1.575 a_p$
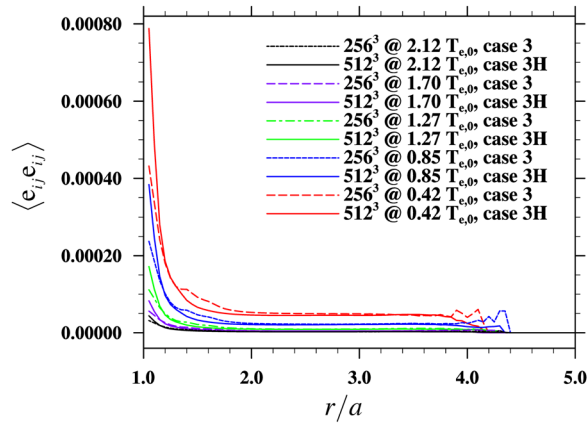
Fig. 11 Profile of bin-averaged $\langle e_{ij}e_{ij}\rangle$ as a function of distance from the particle center, obtained from two grid resolutions

and negative for $r < 1.575a_p$, therefore, energy is provided by forcing mainly away from the particle surface and dissipated mainly near the particle surface within 57.5% of the radius.

Next, we examine the two turbulent transport terms (the first two terms on the right-hand side of Eq. (22)) in Fig. 7. The relative transport is always positive, while the transport of cross-energy is mostly negative. However, near the particle surface, they both become positive. The sum of the two terms is also shown in Fig. 7, which is only weakly positive away from the particle surface. Near the particle surface, the sum is peaked at $r = 1.225a_p$, showing that the turbulent transport pumps kinetic energy mainly to regions near the particle surface. The volume-integrated value of these two turbulent transport terms together is 0.773 in LBM units. This may be interpreted alternatively as the net transport from large-scale turbulent eddies to the small-scale eddies that can provide kinetic energy at the particle scale.

The viscous stress work is shown in Fig. 8, showing a nonmonotonic behavior. In a Stokes disturbance flow (see Fig. 14 in the Appendix), the viscous stress work is always positive and provides kinetic energy to the disturbance flow. In the turbulent flow, for the intermediate region $1.225 < r/a_p < 1.725$, the viscous stress against the relative fluid motion does generate kinetic energy, and it is peaked at $r = 1.325a_p$. However, away from the particle surface, it is weakly negative, meaning the viscous stress work extracts kinetic energy. Very close to the surface $(r \leq 1.225a_p)$, this term becomes strongly negative, meaning that the viscous stress work removes kinetic energy for a moving particle suspended in a turbulent flow. Further study is needed to understand exactly how these negative contributions occur. The volume-integrated value of the viscous stress work is in fact negative and is equal to -0.507 in LBM units.

The only term that remains to be covered is the pressure work term. Unfortunately, direct calculation of the pressure work gives a very oscillatory curve due to artificial acoustic waves in the LBM approach, which tend to become strong near the particle surface. Improved implementations at the moving fluid–particle interfaces are being investigated [29] and will be used in future simulations. Here, we simply derive the pressure work term by assuming that all the terms on the right-hand side balance. The result is shown in Fig. 9, along with other terms for comparison. The pressure work is positive near the particle surface and is the dominant term to balance the viscous dissipation. Away from the surface $(r > 1.425a_p)$, it is negative. The volume-integrated value of the pressure work is equal to 0.604 in LBM units.

In summary, the above results and discussions highlight some interesting dynamics near the particle surface. The viscous dissipation is significantly augmented near the particle surface. The forcing term provides energy in regions away from the particle surface, with the pressure work, the viscous stress work, and the

turbulent transport move the energy into regions near the particle surface. It should be noted that the amount of grid nodes in each bin first increases with r, reaches a peak at $r/a_p = 1.725$, and then decreases quickly, as shown in Fig. 10(a) where the PDF of the number of node points in each bin is plotted. Figure 10(a) shows a much more accurate result in the tail region due to the average over time, when compared to Fig. 7(a) in Ref. [25]. In the tail region, a power-law decay of the PDF is clearly seen. We then replotted Fig. 9 in Fig. 10(b) by weighting the values in Fig. 9 with the PDF. In this manner and with the normalization previously applied, the area between the dissipation rate curve and the zero line is one. The integrals for each curve represent the relative contribution of each term, as noted in the above. All terms make little contribution for $r > 3.5a_p$. In this manner, the forcing energy input is peaked at $r/a_p = 1.775$. The main balance is between the forcing, the pressure term, and the viscous dissipation. The viscous stress work and the turbulent transport make some contributions only very close to the particle surface.

4.3 Particle-Laden Decaying Turbulence. Now, we consider a decaying homogeneous and isotropic turbulence laden with monodisperse, nonsedimenting solid particles simulated in Ref. [24]. We consider one physical case discussed in Ref. [24] but simulated at two grid resolutions. The single-phase flow was first evolved until the velocity-derivative skewness is realistic. Then, solid particles are released into the flow. The parameters of these two simulations are shown in Table 2 at the time of particle release. The two cases are denoted as case 3 and case 3H following Gao et al. [24]. It is noted that the particle radius is resolved by 4 or 8 lattice units, respectively. Initially, the domain is
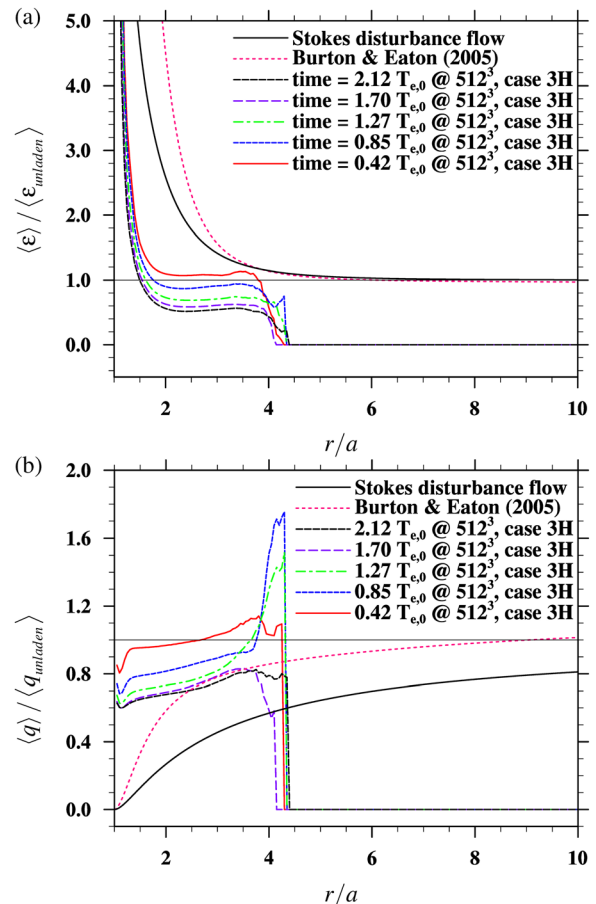

Fig. 12 The normalized (a) dissipation rate and (b) turbulent kinetic energy as a function of the distance from the center of the nearest solid particle. The horizontal line marks the level of 1.0.

12 times the longitudinal integral length (see Table 3 in Ref. [24]). The simulations covered 5000 lattice time steps or 2.12 eddy turnover time (defined at the initial time).

Figure 11 shows the profile of bin-averaged $\langle e_{ij}e_{ij}\rangle = \langle\varepsilon\rangle/2\nu$ computed at five different times for both cases. Again a bin width of $0.05a_p$ is used. The ratio of the averaged particle center-to-center distance to the particle radius is again about 3.47. It is clear that for a given time, the $\langle e_{ij}e_{ij}\rangle$ value decreases rapidly from the surface of a particle to a distance of about $1.5a_p$ and then retains a constant bulk value. This indicates that the main impact of the solid particles on the carrier turbulence occurs within 50% of the particle radius. For both cases 3 and case 3H, the magnitude of $\langle e_{ij}e_{ij}\rangle$ decreases with time, which is expected for decaying turbulent flow simulations. We also noted that the higher resolution (case 3H) yields smoother profiles, e.g., the fluctuations seen in case 3 within the range of $1.3a_p < r < 1.8a_p$ are avoided in case 3H, due to larger number of fluid nodes available in the latter case. For this reason, we will focus only on the results from case 3H for the following discussions.

Figure 12(a) shows the profile of normalized bin-averaged dissipation rate at different times for case 3H. The normalization is performed by scaling the dissipation rate of the particle-laden turbulence with its particle-free counterpart simulated with the same initial condition and lattice resolution. The trends are similar to those found in Fig. 11: the normalized dissipation rate drops substantially within a short distance ($r \approx 1.5a_p$) from the particle surface and decreases with time for decaying turbulence. Again, the results are compared with the averaged data from Fig. 17 in Ref. [14], as well as results from the Stokes disturbance flow
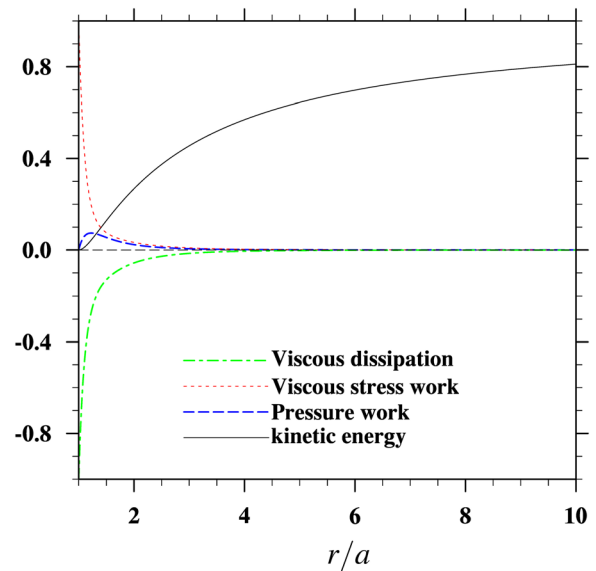
Fig. 14 Profiles conditioned on the particle surface for the Stokes disturbance flow

model. Due to a much larger particle size ($d_p = 16.1\eta$) as compared to what used in Ref. [14] ($d_p = 2.0\eta$), the boundary layer of the fluid flow relative to the solid particle surface is much thinner than the case in Ref. [14]. The particle–particle interactions also contribute to the difference between the two.

Figure 12(b) shows the profile of bin-averaged turbulent kinetic energy as a function of distance from the center of a solid particle. Again, the results are normalized by those from unladen turbulence and are compared with the averaged data from Fig. 16 of Burton and Eaton [14], as well as with the data from an analytic model based on Stokes disturbance flow (Appendix). The turbulent kinetic energy first decreases to a lower value for $r < 1.1a_p$, followed by a rapid increase to a high value at about $r = 1.3a_p$, and then reaches a plateau with a gradual increase till $r \approx 3.5a_p$, after which the results are no longer accurate due to the lack of sufficient number of fluid lattice nodes. As time evolves, the normalized kinetic energy decreases, due to flow decay by viscous dissipation. In addition, the kinetic energy values are in general higher than those from Burton and Eaton [14], due to the difference in particle sizes as mentioned above and also the particles are themselves moving here. For the similar reasons, the Stokes flow model underpredicts the turbulent kinetic energy.

Figure 13 shows that both the dissipation rate and kinetic energy profiles are self-similar when each is normalized by the respective field mean in the particle-laden flow. The dissipation rate profiles have a better self similarity near the particle surface. Such a self-similarity property is useful for model development of the turbulence modulation in the future.

5 Summary and Outlook

Recently, PRSs of turbulent particle-laden flow have become feasible, using both the macroscopic N–S equation [18,19,22,30] and the mesoscopic lattice Boltzmann equation [24–28]. In each approach, the physical accuracy of the computational treatment of the moving fluid–solid interfaces will continue to be improved [29,34], and direct intercomparison between two different approaches serves as a way to build up fidelity of a PRS tool [28]. In this work, we utilized the mesoscopic LBM to resolve the turbulent flow and the suspended solid particles. We first consider the case of a fixed particle in a forced homogeneous isotropic turbulence previously considered by Burton and Eaton [14]. Although we used a much smaller domain size due to computational cost considerations, we were able to reproduce the similar
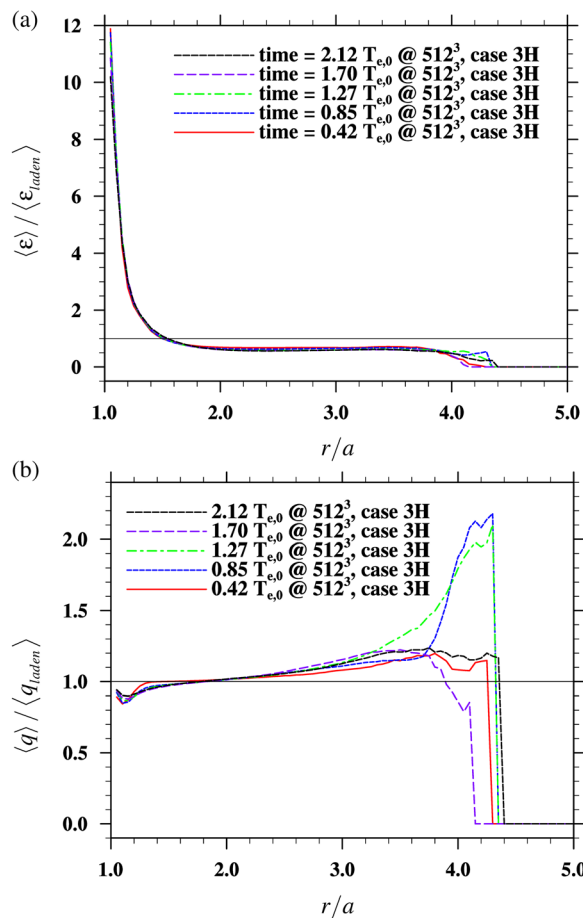

Fig. 13 Profiles of bin-averaged (a) dissipation rate and (b) turbulent kinetic energy as a function of distance from the center of a particle. Each is normalized by the field mean of the particle-laden flow at the same time instant.

results. Specifically, the viscous dissipation profile was shown to be essentially the same as in Ref. [14].

At the same time, new ways of analyzing the simulated flows to better understand flow modulation and particle dynamics are needed. In this paper, we focus on local profiles conditioned on the surface of a solid particle, as in principle, such profiles can be used as a basis to describe the overall turbulence statistics due to the presence of solid particles (e.g., see Fig. 10). They can also provide a way to quantify the effect of embedded solid particle surface. This paper perhaps is the first serious attempt to obtain such local profiles and the related transport processes relevant to the local fluid kinetic energy. We have developed a governing equation to investigate the distribution and transport in the radial direction relative to a moving solid particle. The equation contains turbulent transport terms, pressure and viscous stress work term, and volumetric viscous dissipation and forcing energy inputs.

Then, we computed the local conditioned profiles for a forced, particle-laden, homogeneous and isotropic turbulence discussed in Ref. [25]. The viscous dissipation is significantly augmented near the particle surface. The large-scale forcing term provides energy in regions away from the particle surface, with the pressure work, the viscous stress work, and the turbulent transport move the energy into regions near the particle surface. Overall, the main balance is between the forcing, the pressure term, and the viscous dissipation. The viscous stress work and the turbulent transport make some contributions only very close to the particle surface.

Finally, we examined briefly the kinetic energy and dissipation rate profiles in a decaying particle-laden turbulent flow. We find that the dissipation rate and kinetic energy profiles conditioned on a particle surface appear to be self-similar when normalized by the respective field mean value at the same time and plotted against r/a_p.

We are currently improving a few implantation details of the LBM approach [29] and applying them to the same cases considered in this paper for more accurate direct simulations of the turbulence fields. Specifically, we will compute the pressure work term directly after the artificial pressure oscillations are suppressed. We are also computing all terms in Eq. (22) for the two cases discussed in Secs. 4.1 and 4.3, so we may compare the various profiles to those in Sec. 4.2. These along with a modeling analysis of turbulence modulation by solid particles, based on the conditional profiles, will be reported in the near future.

Acknowledgment

Nomenclature

a, a_p = radius of solid particles
c_s = speed of sound
d, d_p = diameter of solid particles
$\mathbf{e}$ = microscopic velocity
$\mathbf{f}$ = microscopic distribution function vector
$\mathbf{F}$ = force acting on a particle
I_p = moment of inertia of a particle
k = wave number

L_B = computational domain size in any direction
L_f = longitudinal integral length scale
$\mathbf{m}$ = microscopic moments vector
$\mathbf{M}$ = transformation matrix from $\mathbf{f}$ to $\mathbf{m}$
M_p = mass of a solid particle
n = particle number density
N = number of grid points in a given spatial direction
p = local fluid pressure
$\mathbf{q}$ = nonuniform force vector per unit mass
$\mathbf{Q}$ = nonuniform force vector in the microscopic velocity space
R_λ = Taylor microscale flow Reynolds number, $R_\lambda = u_{\mathrm{rms}}\lambda/\nu$
s_{ij} = strain rate tensor
$\mathbf{S}$ = relaxation matrix
$\mathbf{T}$ = torque acting on a particle
T_e = eddy turnover time
u = fluid velocity in the x direction
u^* = friction velocity
v = fluid velocity in the y direction
$\mathbf{V}$ = particle velocity
w = fluid velocity in the z direction
$\mathbf{Y}$ = particle position
$\delta\rho$ = density fluctuations in LBM
ε = viscous dissipation rate
η = Kolmogorov scale
Θ = particle angular position
λ = Taylor microscale
δt = time step size
ν = fluid kinematic viscosity
ρ, ρ_f = fluid density
ρ_p = density of solid particles
ϕ_v = average particle volume fraction
Ω_p = particle angular velocity

Subscripts

i, j = spatial direction indices
p = solid or the particulate phase
pl = quantities associated with a particle-laden flow
r = radial direction in spherical coordinates
rms = root-mean-squared value
sp = quantities associated with a single-phase flow
α = microscopic lattice velocity direction, from 0 to 18
θ = polar angle in spherical coordinates
ϕ = azimuthal angle in spherical coordinates

Superscripts

$^{(\mathrm{eq})}$ = value corresponding to equilibrium
^{P} = average over all particles
^{S} = average over a spherical surface at a given r
^{T} = average over time
$^{-1}$ = inverse matrix

Appendix: Profiles Conditioned on Particle Surface for Stokes Disturbance Flow

It may be instructive to examine the profiles conditioned on the particle surface for the Stokes disturbance flow. Relative to the spherical particle, the Stokes disturbance flow, velocity field, and pressure field may be written in spherical coordinates as

$$u_r = V\left(1 - \frac{3a}{2r} + \frac{a^3}{2r^3}\right)\cos\theta, \quad u_\theta = -V\left(1 - \frac{3a}{4r} - \frac{a^3}{4r^3}\right)\sin\theta,$$

$$u_\phi = 0, \quad p = -\frac{3a\mu V\cos\theta}{2r^2} \tag{A1}$$

where V is the far field flow velocity relative to the solid particle, and the radius of the particle is now donated by a. In this case, Eq. (22) is simplified to only three terms, pressure work, viscous work, and viscous dissipation

$$0 = -\left[\frac{1}{r^2}\frac{\partial}{\partial r}\left(r^2\left\langle\frac{pu_r}{\rho_f}\right\rangle^S\right)\right] + \left[\frac{1}{r^2}\frac{\partial}{\partial r}\left(r^2\langle 2\nu\mathbf{u}\cdot\mathbf{e}\rangle^S\right)\right] - \langle\varepsilon\rangle^S$$

(A2)

The kinetic energy profile is

$$\left\langle\frac{1}{2}u^2\right\rangle^S = \frac{1}{4\pi r^2}\int_0^\pi \frac{1}{2}\left(u_r^2 + u_\theta^2\right)2\pi r^2\sin\theta d\theta$$
$$= \frac{V^2}{2}\left(1 - \frac{2a}{r} + \frac{9a^2}{8r^2} - \frac{a^4}{4r^4} + \frac{a^6}{8r^6}\right)$$

(A3)

which increases monotonically from zero at the surface $r/a = 1$ to the ambient value at $r/a \to \infty$.

In spherical polar coordinates, the components of the strain rate tensor for the Stokes disturbance flow take the form

$$s_{rr} = \frac{\partial u_r}{\partial r} = V\cos\theta\left(-\frac{3a^3}{2r^4} + \frac{3a}{2r^2}\right)$$

(A4)

$$s_{\theta\theta} = \frac{1}{r}\frac{\partial u_\theta}{\partial\theta} + \frac{u_r}{r} = V\cos\theta\left(\frac{3a^3}{4r^4} - \frac{3a}{4r^2}\right)$$

(A5)

$$s_{\varphi\varphi} = \frac{1}{r\sin\theta}\frac{\partial u_\varphi}{\partial\varphi} + \frac{u_r}{r} + \frac{u_\theta\cot\theta}{r} = V\cos\theta\left(\frac{3a^3}{4r^4} - \frac{3a}{4r^2}\right)$$

(A6)

$$s_{\theta\varphi} = \frac{\sin\theta}{2r}\frac{\partial}{\partial\theta}\left(\frac{u_\varphi}{\sin\theta}\right) + \frac{1}{2r\sin\theta}\frac{\partial u_\theta}{\partial\varphi} = 0$$

(A7)

$$s_{\varphi r} = \frac{1}{2r\sin\theta}\frac{\partial u_r}{\partial\varphi} + \frac{r}{2}\frac{\partial}{\partial r}\left(\frac{u_\varphi}{r}\right) = 0$$

(A8)

$$s_{r\theta} = \frac{r}{2}\frac{\partial}{\partial r}\left(\frac{u_\theta}{r}\right) + \frac{1}{2r}\frac{\partial u_r}{\partial\theta} = -V\sin\theta\frac{3a^3}{4r^4}$$

(A9)

Then, the local dissipation rate is

$$\varepsilon \equiv 2\nu s_{ij}s_{ij}$$
$$= \frac{\nu V^2}{r^2}\left(\frac{3}{2}\right)^2\left\{\cos^2\theta\left[3\left(\frac{a}{r}\right)^2 - 6\left(\frac{a}{r}\right)^4 + 2\left(\frac{a}{r}\right)^6\right] + \left(\frac{a}{r}\right)^6\right\}$$

(A10)

Therefore, the dissipation rate profile is

$$\langle\varepsilon\rangle^S = \frac{1}{4\pi r^2}\int_0^\pi \varepsilon(r,\theta)\,2\pi r^2\sin\theta d\theta = \frac{3}{2}\frac{\nu V^2}{a^2}\left[\frac{3a^2}{2r^2} - \frac{3a^4}{r^4} + \frac{5a^6}{2r^6}\right]\frac{a^2}{r^2}$$

(A11)

which decreases monotonically from the maximum of $3\nu V^2/2a^2$ at the surface $r/a = 1$ to zero at $r/a \to \infty$.

The shell-averaged value of the pressure work term is

$$-\left[\frac{1}{r^2}\frac{\partial}{\partial r}\left(r^2\left\langle\frac{pu_r}{\rho_f}\right\rangle^S\right)\right] = \frac{3}{2}\frac{\nu V^2}{a^2}\left[\frac{a^2}{2r^2} - \frac{a^4}{2r^4}\right]\frac{a^2}{r^2}$$

(A12)

which is zero at both the surface and $r/a \to \infty$. A maximum value occurs at $r/a = 1.5$.

The shell-averaged value of viscous stress work is

$$\left[\frac{1}{r^2}\frac{\partial}{\partial r}\left(r^2\langle 2\nu\mathbf{u}\cdot\mathbf{e}\rangle^S\right)\right] = \frac{3}{2}\frac{\nu V^2}{a^2}\left[\frac{a^2}{r^2} - \frac{5a^4}{2r^4} + \frac{5a^6}{2r^6}\right]\frac{a^2}{r^2}$$

(A13)

which decreases monotonically from the maximum of $3\nu V^2/2a^2$ at the surface $r/a = 1$ to zero at $r/a \to \infty$.

Together, we confirm that the three terms are balanced. The total viscous dissipation over the whole fluid region is $6\pi\nu aV^2$, which is balanced by the total pressure work of $2\pi\nu aV^2$ and total viscous stress work of $4\pi\nu aV^2$. Figure 14 shows these profiles as a function of r/a.

When applied to a turbulent flow, we match the far field value of the Stokes flow to the value in a single-phase turbulence (i.e., without particles). A model based on Eq. (A3) is

$$\frac{\langle q^2\rangle}{\langle q_{ul}^2\rangle} = \frac{1}{4\pi r^2}\int_0^\pi \frac{1}{2}\left(u_r^2 + u_\theta^2\right)2\pi r^2\sin\theta d\theta$$
$$= \frac{V^2}{2}\left(1 - \frac{2a}{r} + \frac{9a^2}{8r^2} - \frac{a^4}{4r^4} + \frac{a^6}{8r^6}\right)$$

(A14)

where $\langle q_{ul}^2\rangle$ is the average value in the single-phase (unladen) turbulence at the same time.

Similarly, the dissipation rate profile, Eq. (A11), is modified for a turbulent background flow as

$$\langle\varepsilon\rangle^S = \frac{3}{2}\frac{\nu V^2}{a^2}\left[\frac{3a^2}{2r^2} - \frac{3a^4}{r^4} + \frac{5a^6}{2r^6}\right]\frac{a^2}{r^2} + \langle\varepsilon_{ul}\rangle$$

(A15)

where the single-phase (unladen) value $\langle\varepsilon_{ul}\rangle$ is added to account for the contribution from the background turbulence. With $\langle\varepsilon_{ul}\rangle$ being defined as $\varepsilon_{ul} = 15\nu u'^2/\lambda^2$, where u' is the rms fluid velocity, λ is the Taylor microscale length, and assuming the slip velocity V is proportional to the rms velocity, i.e., $V = \beta u'$ with β as a fitting parameter, we then have

$$\frac{\langle\varepsilon\rangle}{\varepsilon_{ul}} = \frac{\beta^2}{20}\left(\frac{\lambda}{r}\right)^2\left[3\left(\frac{a}{r}\right)^2 - 6\left(\frac{a}{r}\right)^4 + 5\left(\frac{a}{r}\right)^6\right] + 1$$

(A16)

References

[1] Balachandar, S., and Eaton, J. K., 2010, "Turbulent Dispersed Multiphase Flow," Annu. Rev. Fluid Mech. **42**(1), pp. 111–133.

[2] Corsini, A., Rispoli, F., Sheard, A. G., and Venturini, P., 2013, "Numerical Simulation of Coal Fly-Ash Erosion in an Induced Draft Fan," ASME J. Fluids Eng., **135**(1), p. 081303.

[3] Patro, P., and Dash, S. K., 2014, "Computations of Particle-Laden Turbulent Jet Flows Based on Eulerian Model," ASME J. Fluids Eng., **136**(1), p. 011301.

[4] Maxey, M. R., and Riley, J. J., 1983, "Equation of Motion for a Small Rigid Sphere in a Nonuniform Flow," Phys. Fluids, **26**(4), pp. 883–889.

[5] Wang, L.-P., Rosa, B., Gao, H., He, G. W., and Jin, G. D., 2009, "Turbulent Collision of Inertial Particles: Point-Particle Based, Hybrid Simulations and Beyond," Int. J. Multiphase Flow, **35**(9), pp. 854–867.

[6] Squires, K. D., and Eaton, J. K., 1991, "Preferential Concentration of Particles by Turbulence," Phys. Fluids A, **3**(5), pp. 1169–1179.

[7] Wang, L.-P., and Maxey, M. R., 1993, "Settling Velocity and Concentration Distribution of Heavy Particles in Homogeneous Isotropic Turbulence," J. Fluid Mech., **256**, pp. 27–68.

[8] Squires, K. D., and Eaton, J. D., 1990, "Particle Response and Turbulence Modification in Isotropic Turbulence," Phys. Fluids A, **2**(7), pp. 1191–1203.

[9] Elghobashi, S., and Truesdell, G., 1993, "On the 2-Way Interaction Between Homogeneous Turbulence and Dispersed Solid Particles. I: Turbulence Modification," Phys. Fluids A, **5**(7), pp. 1790–1801.

[10] Sundaram, S., and Collins, L. R., 1997, "Collision Statistics in an Isotropic Particle-Laden Turbulent Suspension. Part 1. Direct Numerical Simulations," J. Fluid Mech., **335**, pp. 75–109.

[11] Zhou, Y., Wexler, A. S., and Wang, L.-P., 2001, "Modeling Turbulent Collision of Bidisperse Inertial Particles," J. Fluid Mech., **433**, pp. 77–104.

[12] Ayala, O., Grabowski, W. W., and Wang, L.-P., 2007, "A Hybrid Approach for Simulating Turbulent Collisions of Hydrodynamically-Interacting Particles," J. Comput. Phys., **225**(1), pp. 51–73.

[13] Jin, G. D., He, G. W., and Wang, L.-P., 2010, "Large Eddy Simulation of Collisional Statistics of Inertial Particles in Isotropic Turbulence," Phys. Fluids., **22**(5), p. 055106.

[14] Burton, T. M., and Eaton, J. K., 2005, "Fully Resolved Simulations of Particle-Turbulence Interaction," J. Fluid Mech., **545**, pp. 67–111.

[15] Gore, R. A., and Crowe, C. T., 1989, "Effect of Particle Size on Modulating Turbulent Intensity," Int. J. Multiphase Flow, **15**(2), pp. 279–285.

[16] Crowe, C. T., 2000, "On Models for Turbulence Modulation in Fluid-Particle Flows," Int. J. Multiphase Flow, **26**(5), pp. 719–727.

[17] Uhlmann, M., 2005, "An Immersed Boundary Method With Direct Forcing for the Simulation of Particulate Flows," J. Comput. Phys. **209**(2), pp. 448–476.

[18] Uhlmann, M., 2008, "Interface-Resolved Direct Numerical Simulation of Vertical Particulate Channel Flow in the Turbulent Regime," Phys. Fluids, **20**(5), p. 053305.

[19] Shao, X., Wu, T., and Yu, Z., 2012, "Fully Resolved Numerical Simulation of Particle-Laden Turbulent Flow in a Horizontal Channel at a Low Reynolds Number," J. Fluid Mech., **693**, pp. 319–344.

[20] Yang, J. M., and Stern, F., 2014, "A Sharp Interface Direct Forcing Immersed Boundary Approach for Fully Resolved Simulations of Particulate Flows," ASME J. Fluids Eng., **136**(4), p. 040904.

[21] Zhang, Z., and Prosperetti, A., 2005, "A Second-Order Method for Three-Dimensional Particle Simulation," J. Comput. Phys., **210**(1), pp. 292–324.

[22] Yeo, K., Dong, S., Climent, E., and Maxey, M. R., 2010, "Modulation of Homogeneous Turbulence Seeded With Finite Size Bubbles or Particles," Int. J. Multiphase Flow, **36**(3), pp. 221–233.

[23] Homann, H., and Bec, J., 2010, "Finite-Size Effects in the Dynamics of Neutrally Buoyant Particles in Turbulent Flow," J. Fluid Mech., **651**, pp. 81–91.

[24] Gao, H., Li, H., and Wang, L.-P., 2013, "Lattice Boltzmann Simulation of Turbulent Flow Laden With Finite-Size Particles," Comput. Math. Appl., **65**(2), pp. 194–210.

[25] Wang, L.-P., Ayala, O., Gao, H., Andersen, C., and Mathews, K., 2014, "Study of Forced Turbulence and Its Modulation by Finite-Size Solid Particles Using the Lattice Boltzmann Approach," Comput. Math. Appl., **67**(2), pp. 363–380.

[26] Gillissen, J., 2013, "Turbulent Drag Reduction Using Fluid Spheres," J. Fluid Mech., **716**, pp. 83–95.

[27] Ten Cate, A., Derksen, J. J., Portela, L. M., and van den Akker, H. E. A., 2004, "Fully Resolved Simulations of Colliding Monodisperse Spheres in Forced Isotropic Turbulence," J. Fluid Mech., **519**, pp. 233–271.

[28] Wang, L.-P., Peng, C., Guo, Z., and Yu, Z., 2015, "Flow Modulation by Finite-Size Neutrally Buoyant Particles in a Turbulent Channel Flow," ASME J. Fluids Eng. (in press).

[29] Peng, C., Teng, Y., Hwang, B., Guo, Z., and Wang, L.-P., 2015, "Implementation Issues and Benchmarking of Lattice Boltzmann Method for Moving Particle Simulations in a Viscous Flow," Comput. Math. Appl. (in press).

[30] Lucci, F., Ferrante, A., and Elghobashi, S., 2010, "Modulation of Isotropic Turbulence by Particles of Taylor Length-Scale Size," J. Fluid Mech., **650**, pp. 5–55.

[31] Chen, S., and Doolen, G., 1998, "Lattice Boltzmann Method for Fluid Flows," Annu. Rev. Fluid Mech., **30**(1), pp. 329–364.

[32] Qian, Y. H., d'Humières, D., and Lallemand, P., 1992, "Lattice BGK Models for Navier–Stokes Equation," Europhys. Lett., **17**(6BIS), pp. 479–484.

[33] d'Humières, D., Ginzburg, I., Krafczyk, M., Lallemand, P., and Luo, L.-S., 2002, "Multiple-Relaxation-Time Lattice Boltzmann Models in Three-Dimensions," Phil. Trans. R. Soc. London A, **360**(1792), pp. 437–451.

[34] Wang, L.-P., Peng, C., Guo, Z., and Yu, Z., 2015, "Lattice Boltzmann Simulation of Particle-Laden Turbulent Channel Flow," Comput. Fluids (in press).

[35] Guo, Z., Zheng, C., and Shi, B., 2002, "Discrete Lattice Effects on the Forcing Term in the Lattice Boltzmann Method," Phys. Rev. E., **65**(4), p. 046308.

[36] Lu, J., Han, H., Shi, B., and Guo, Z., 2012, "Immersed Boundary Lattice Boltzmann Model Based on Multiple Relaxation Times," Phys. Rev. E, **85**(1), p. 016711.

[37] Lallemand, P., and Luo, L.-S., 2003, "Lattice Boltzmann Method for Moving Boundaries," J. Comp. Phys., **184**(2), pp. 406–421.

[38] Chen, L., Yu, Y., Lu, J., and Hou, G., 2014, "A Comparative Study of Lattice Boltzmann Methods Using Bounce-Back Schemes and Immersed Boundary Ones for Flow Acoustic Problems," Int. J. Numer. Meth. Fluids, **74**(6), pp. 439–467.

[39] Wen, B., Zhang, C., Tu, Y., Wang, C., and Fang, H., 2014, "Galilean Invariant Fluid-Solid Interfacial Dynamics in Lattice Boltzmann Simulations," J. Comput. Phys., **266**, pp. 161–170.

[40] Nguyen, N. Q., and Ladd, A. J. C., 2002, "Lubrication Corrections for Lattice-Boltzmann Simulations of Particle Suspensions," Phys. Rev. E, **66**(4), p. 046708.

[41] Dance, S. L., and Maxey, M. R., 2003, "Incorporation of Lubrication Effects Into the Force-Coupling Method for Particulate Two-Phase Flow," J. Comput. Phys., **189**(1), pp. 212–238.

[42] Peng, Y., Liao, W., Luo, L.-S., and Wang, L.-P., 2010, "Comparison of the Lattice Boltzmann and Pseudo-Spectral Methods for Decaying Turbulence: Low-Order Statistics," Comput. Fluids, **39**(4), pp. 568–591.

[43] Crowe, C. T., Schwarzkopf, J. D., Sommerfeld, M., and Tsuji, Y., 2012, *Multiphase Flows With Droplets and Particles*, 2nd ed., CRC Press, Boca Raton.

[44] Fox, R. O., 2012, "Large-Eddy-Simulation Tools for Multiphase Flows," Annu. Rev. Fluid Mech., **44**(1), pp. 47–76.

[45] Mei, R., Luo, L.-S., Lallemand, P., and d'Humières, D., 2006, "Consistent Initial Conditions for Lattice Boltzmann Simulations," Comput. Fluids, **35**(8–9), pp. 855–862.

[46] Yu, H., Luo, L.-S., and Girimaji, S. S., 2006, "LES of Turbulent Square Jet Flow Using an MRT Lattice Boltzmann Model," Comput. Fluids, **35**(8–9), pp. 957–965.